Electronic Supplementary Material (ESI) for Energy & Environmental Science.

--Supplementary Information--

How alkali cations affect salt precipitation and CO_2 electrolysis performance in membrane electrode assembly CO_2 electrolyzers

Sahil Garg [a, †], Qiucheng Xu[a, †], Asger B. Moss[a], Marta Mirolo[b], Wanyu Deng[a], Ib Chorkendorff[a], Jakub Drnec[b], Brian Seger[a, *]

[a]*Surface Physics and Catalysis (Surf Cat) Section, Department of Physics, Technical University of Denmark, 2800 Kgs. Lyngby, Denmark*

[b]*Experimental Division, European Synchrotron Radiation Facility, Grenoble, France*

[†]*Joint first authors: Sahil Garg; Qiucheng Xu*

**Corresponding author: Brian Seger, Email: brse@fysik.dtu.dk*

Supplementary Note 1: Detailed analysis of cation effect on CO_2E over Cu GDEs used in MEA electrolyzer

In literature, the effect of alkali cations on CO_2E is extensively studied,[1-3] however, there are no exclusive studies[4] reported on cation's effect in a MEA electrolyzer (especially over Cu GDEs). The CO_2RR selectivity trends shown in Figure 2a match very well with the CO_2E studies conducted in H-cell[5, 6] and catholyte-based electrolyzers.[7, 8] The local environment at the cathode in MEA is completely different than in aqueous electrolyte systems where water is in abundant amount (55 M) and the cathode becomes CO_2 mass transport limited at current densities > 10 $mA \cdot cm^{-2}$ for H-cell,[9, 10] and current densities > 100 $mA \cdot cm^{-2}$ for catholyte-based electrolyzer.[11] However, in MEA electrolyzers, water concentration decreases, and CO_2 supply remains higher (close to its saturation limit) even at current densities ~ 1000 $mA \cdot cm^{-2}$.[12] Our additional experiments performed at lower current densities (25 $mA \cdot cm^{-2}$) and constant cell potential (2.75 V) show similar HER and CO2RR selectivity trends (see Figures S2 and S3) to what we observe in Figure 2a; the only difference is higher production of C_1 products (CO and formate) at low overpotentials while ethylene takes over at higher overpotentials. Between (Na/K/Cs)HCO_3, the electrolyzer operates at similar cell potential (regardless of current density), however, a slightly higher cell potential (> 50 mV, Figure S1) with $NaHCO_3$ leads to higher methane (see Figure 2a and S2) which in general has a slightly higher onset potential.[13]

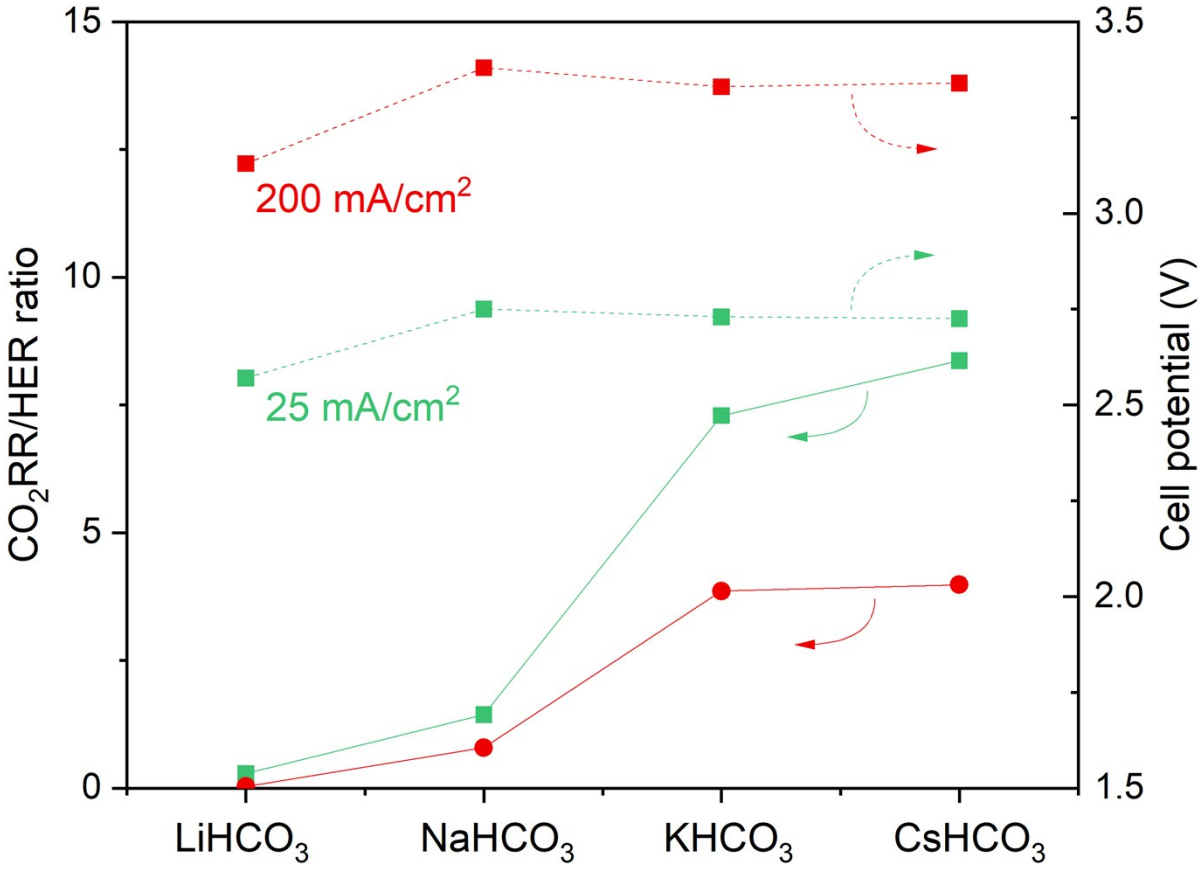

Figure S1. Comparison of CO_2RR/ HER ratio (left y-axis) and cell potential (right y-axis) over different alkali cations at 25 and 200 mA·cm^{-2}. All tests were performed for around 1 h using a fresh set of cathodes, anode, and AEM. The data shown are without X-rays (performed at DTU lab).

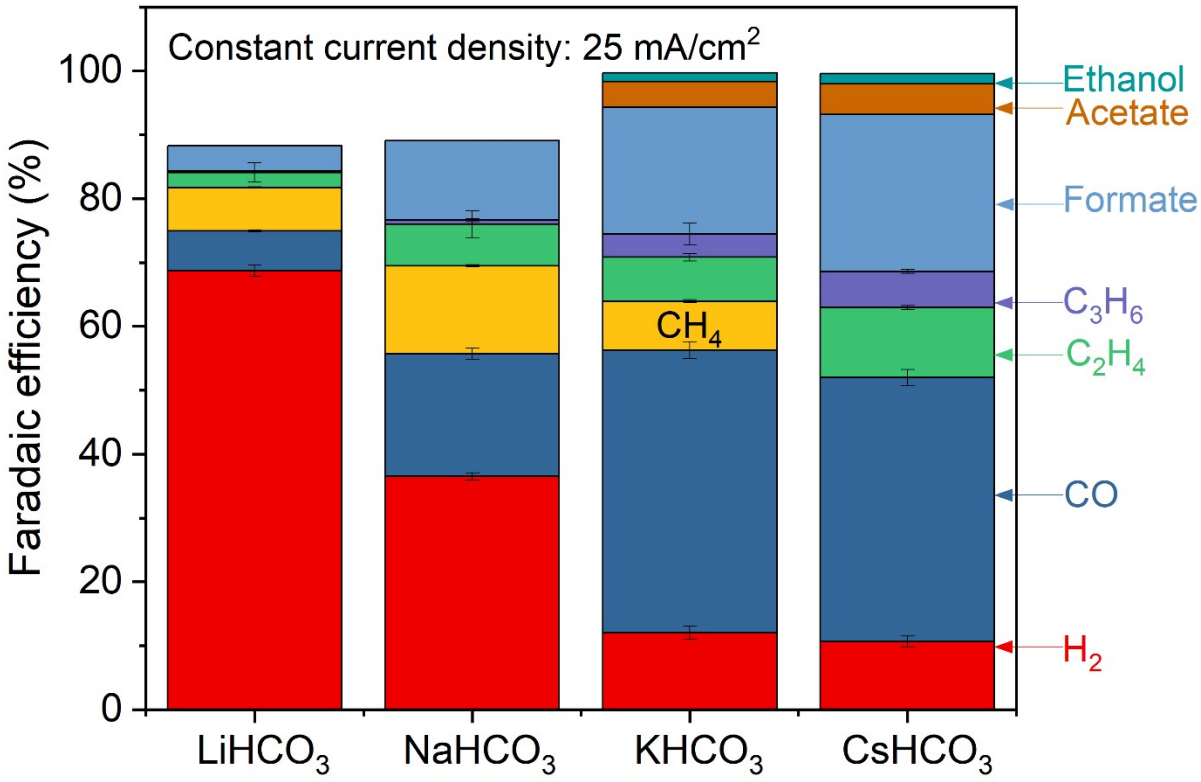

Figure S2. Changes in CO_2RR and HER selectivity with 0.1 M $MHCO_3$ anolyte (where M could be Li, Na, K, and Cs) at 25 $mA \cdot cm^{-2}$. All tests were performed for around 1 h using a fresh set of cathode, anode, and AEM. The data shown are without X-rays (performed at DTU lab).

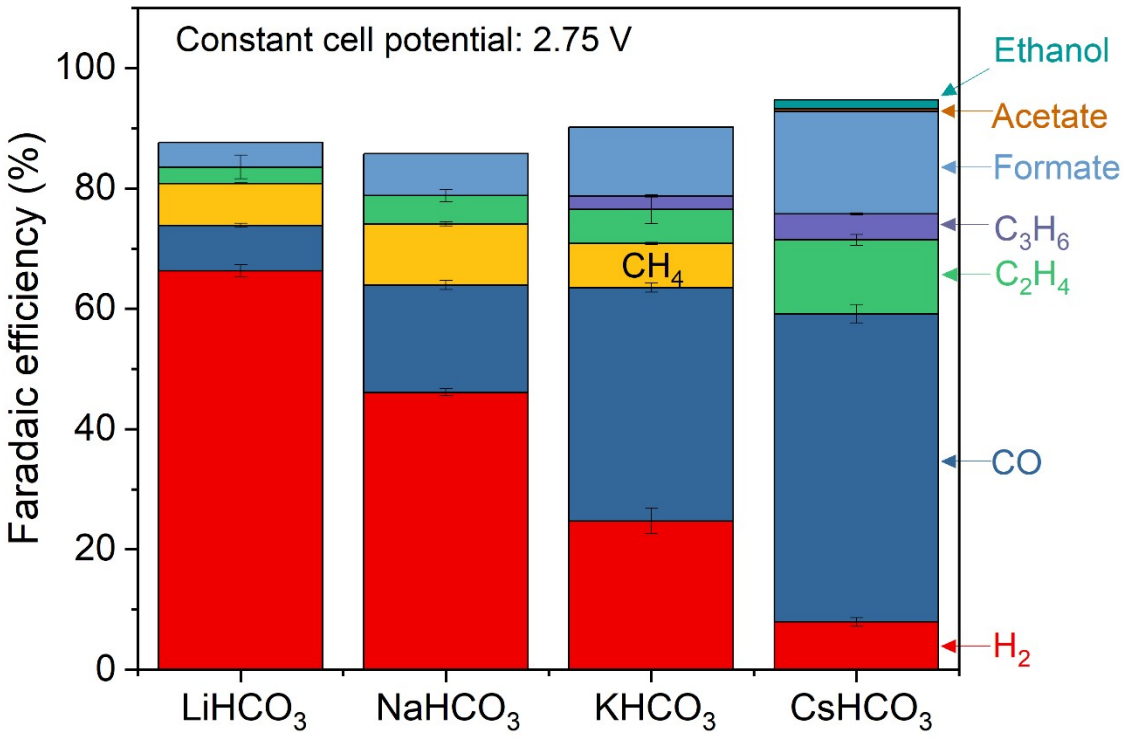

Figure S3. Changes in CO_2RR and HER selectivity with 0.1 M $MHCO_3$ anolyte (where M could be Li, Na, K, and Cs) at 2.75 V (without any *iR* correction). All tests were performed for around 1 h using a fresh set of cathode, anode, and AEM. The data shown are without X-rays (performed at DTU lab).

Supplementary Note 2: CO_2/O_2 ratio at the anode

To understand CO_2 evolving at the anode along with oxygen evolution reaction, we look at different reactions happening both at the cathode and anode during CO_2 electrolysis, The reduction reactions at the cathode result in the production of OH^- ions (as shown in reactions S1 and S2). These OH^- ions then react with the feed CO_2 to form HCO_3^- or CO_3^{2-} (as depicted in reactions S3 and S4).

Reduction reactions at the cathode

$$\alpha CO_2 + \beta H_2O + ne^- \rightarrow C_xH_yO_z + nOH^- \quad \text{(S1)}$$

$$2H_2O + 2e^- \rightarrow H_2 + 2OH^- \quad \text{(S2)}$$

Homogenous buffer reactions at the cathode

$$CO_2 + OH^- \leftrightarrow HCO_3^- \quad (pK_a = 7.8) \quad \text{(S3)}$$

$$OH^- + HCO_3^- \leftrightarrow CO_3^{2-} \quad (pK_a = 10.3) \quad \text{(S4)}$$

The anions including OH^-, HCO_3^- or CO_3^{2-} will subsequently diffuse towards the anode via the anion exchange membrane as ion-carriers. The anodically produced protons (as shown in reaction S5) then neutralizes these diffused anions to form water and/or evolve CO_2 at the anode (see reactions S6 to S8).

Oxidation reaction at the anode

$$2H_2O \rightarrow O_2 + 4H^+ + 4e^- \quad \text{(S5)}$$

Homogenous neutralization reactions at the anode

$$OH^- + H^+ \rightarrow H_2O \quad \text{(S6)}$$

$$HCO_3^- + H^+ \rightarrow CO_2 + H_2O \quad \text{(S7)}$$

$$CO_3^{2-} + 2H^+ \rightarrow CO_2 + H_2O \quad \text{(S8)}$$

By combining the oxidation reaction S5 with homogenous reactions S6 to S8, we will obtain the equations S9 to S11, which clearly explains that when there is pure OH^- transfer through the AEM, the CO_2/O_2 ratio is 0; when it is pure HCO_3^- transfer, the ratio should be 4 while it should be 2 when CO_3^{2-} are the ion carriers through the AEM.

$$4OH^- \rightarrow 2H_2O + O_2 + 4e^- \quad \text{(S9)}$$

$$4HCO_3^- \rightarrow 4CO_2 + 2H_2O + O_2 + 4e^- \quad \text{(S10)}$$

$$CO^2{}_3^- \rightarrow 2CO_2 + O_2 + 4e^- \quad \text{(S11)}$$

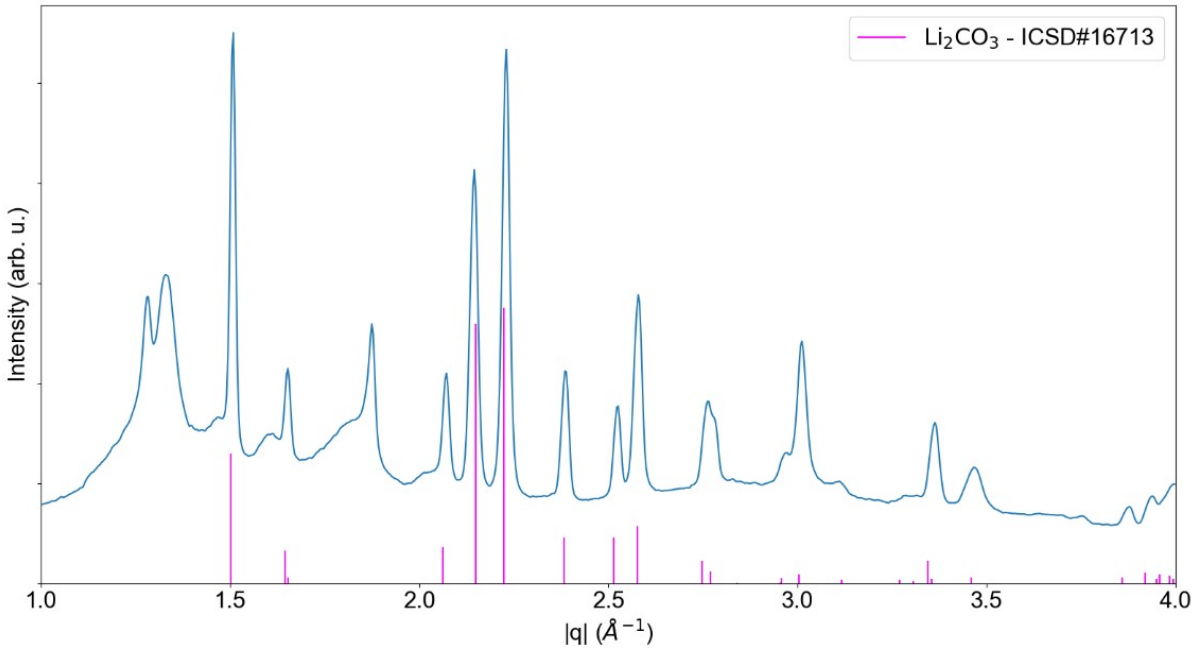

Figure S4. Single pattern with Li_2CO_3 present as salt on the Cu catalyst layer. Reference patterns for Li_2CO_3 (magenta) are shown below.

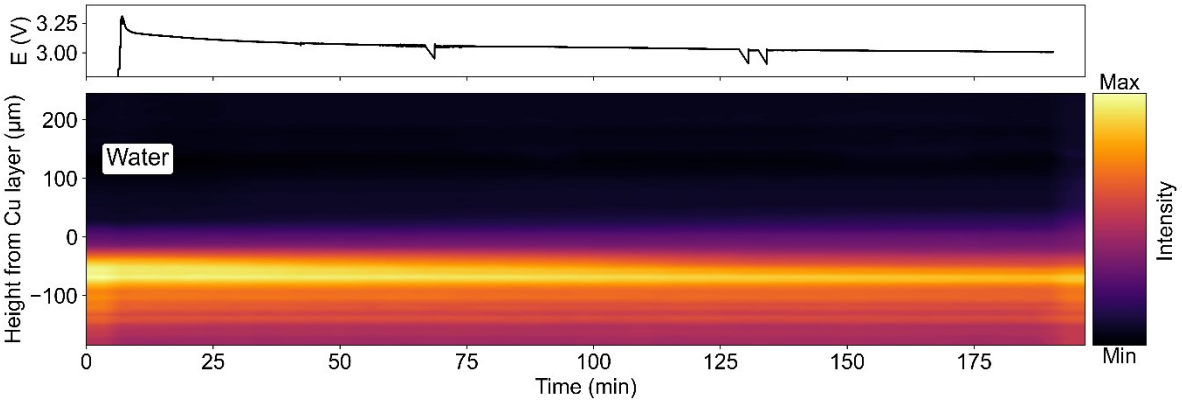

Figure S5. Change in cell potential (top) and background intensity (meaning a change in electrolyte content, bottom plot) in the MEA over electrolysis time. The experiment was performed at 200 $mA \cdot cm^{-2}$ and in 0.1 M $LiHCO_3$ anolyte (same as the one shown in Figure 3).

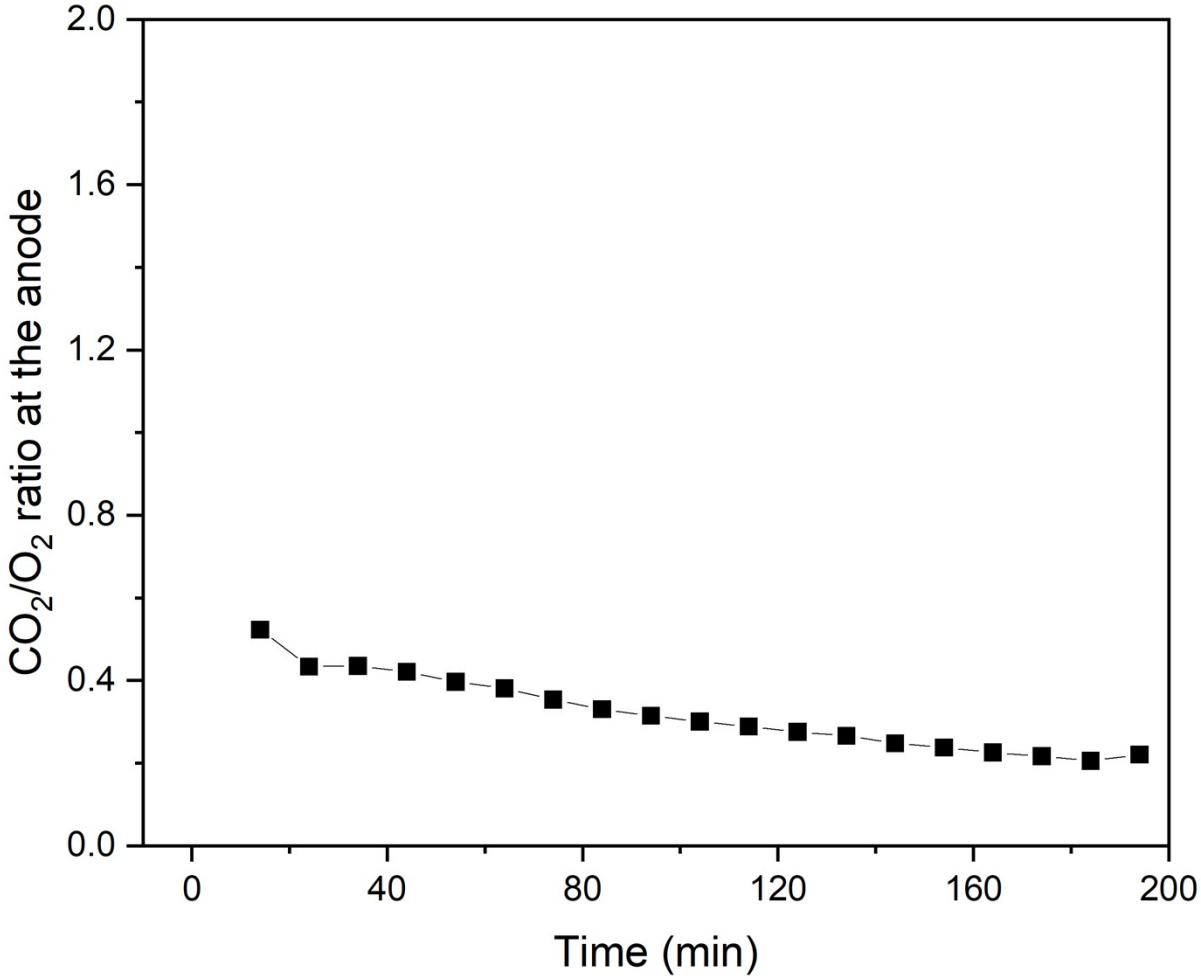

Figure S6. Changes in CO_2/O_2 ratio at the anode outlet as a function of electrolysis time. The experiment was performed at 200 $mA \cdot cm^{-2}$ and in 0.1 M $LiHCO_3$ anolyte (same as the one shown in Figure 3).

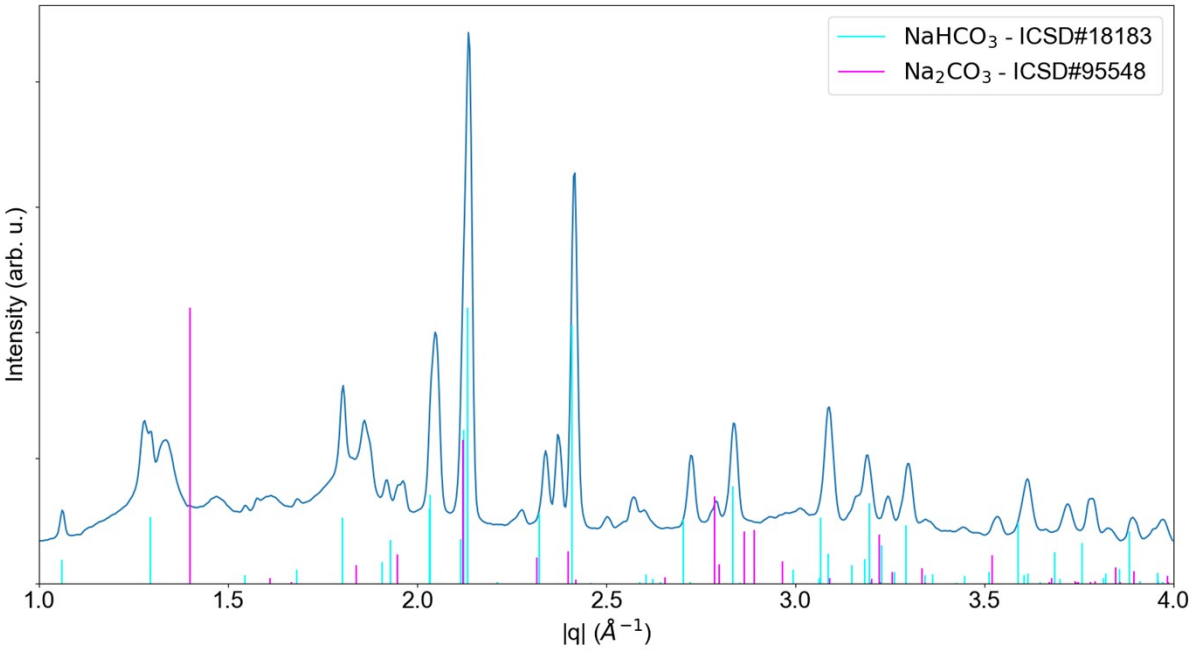

Figure S7. Single pattern with $NaHCO_3$ present as salt in the GDE. Reference patterns for $NaHCO_3$ (cyan) and Na_2CO_3 (magenta) are shown below.

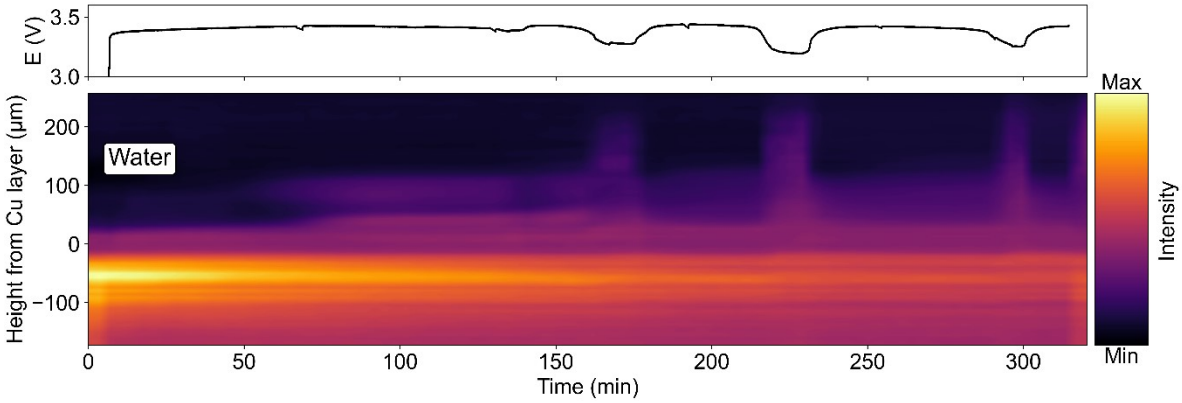

Figure S8. Change in cell potential (top plot) and background intensity (meaning a change in electrolyte content, bottom plot) near the catalyst surface over electrolysis time. The experiment was performed at 200 $mA \cdot cm^{-2}$ and in 0.1 M $NaHCO_3$ anolyte (same as the one shown in Figure 4).

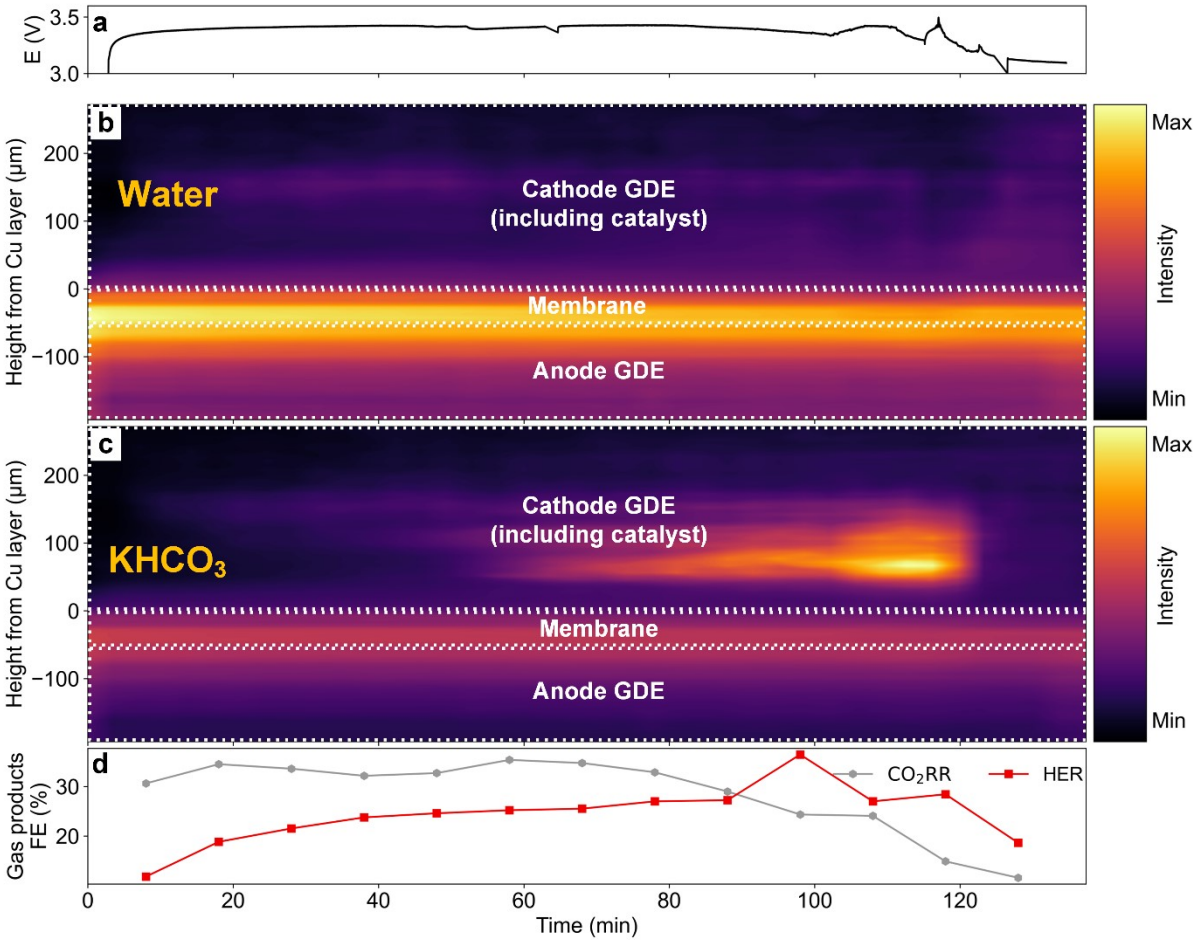

Figure S9. Changes in (a) cell potential, (b) electrolyte/water evolution, (c) salt precipitation, and (d) gaseous CO_2RR/HER selectivity in the MEA over electrolysis time. The experiment was performed at 200 mA·cm^{-2} and in 0.1 M $KHCO_3$ anolyte. The color intensities shown in (b) and (c) are not comparable with each other and should be treated separately.

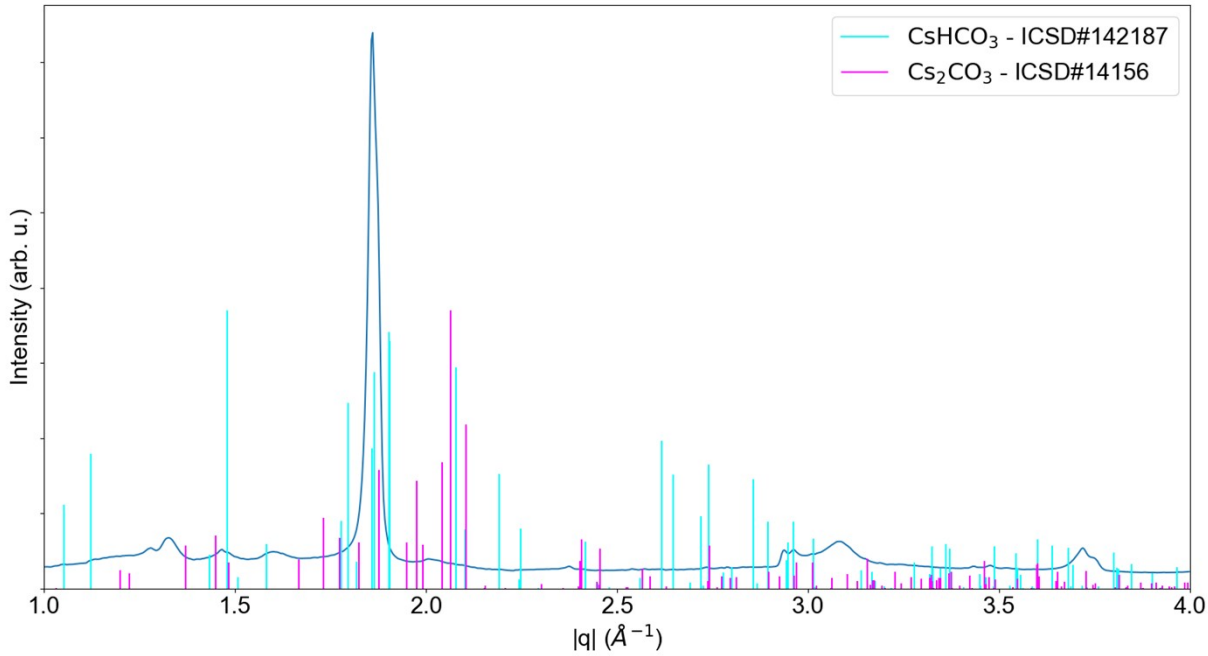

Figure S10. Single pattern showing where salt peaks could be observed if there is any salt precipitation in the GDE with reference patterns for $CsHCO_3$ (cyan) and Cs_2CO_3 (magenta) are shown below.

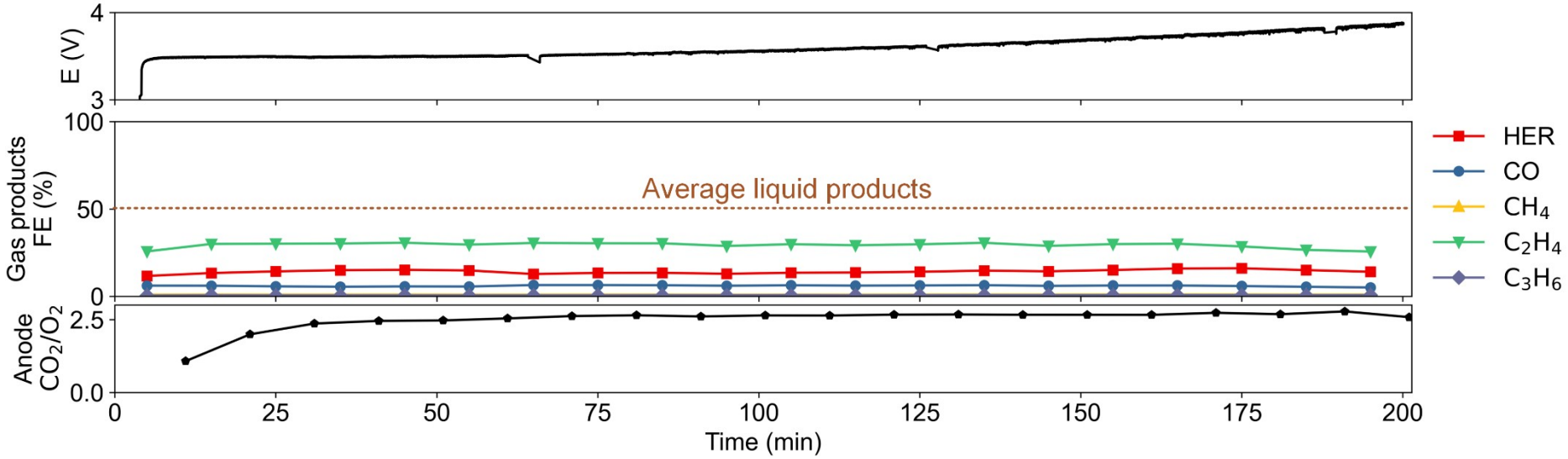

Figure S11. Changes in cell potential (top plot), CO_2RR/HER selectivity (middle plot), and CO_2/O_2 ratio at the anode (bottom plot) over electrolysis time. The experiment was performed at 200 mA·cm^{-2} and in 0.1 M $CsHCO_3$ anolyte (the same as shown in Figure 5 of the main manuscript). The brown dotted liquid in middle plot refers to the average selectivity of liquid products (see Table S4 for detailed liquid product data).

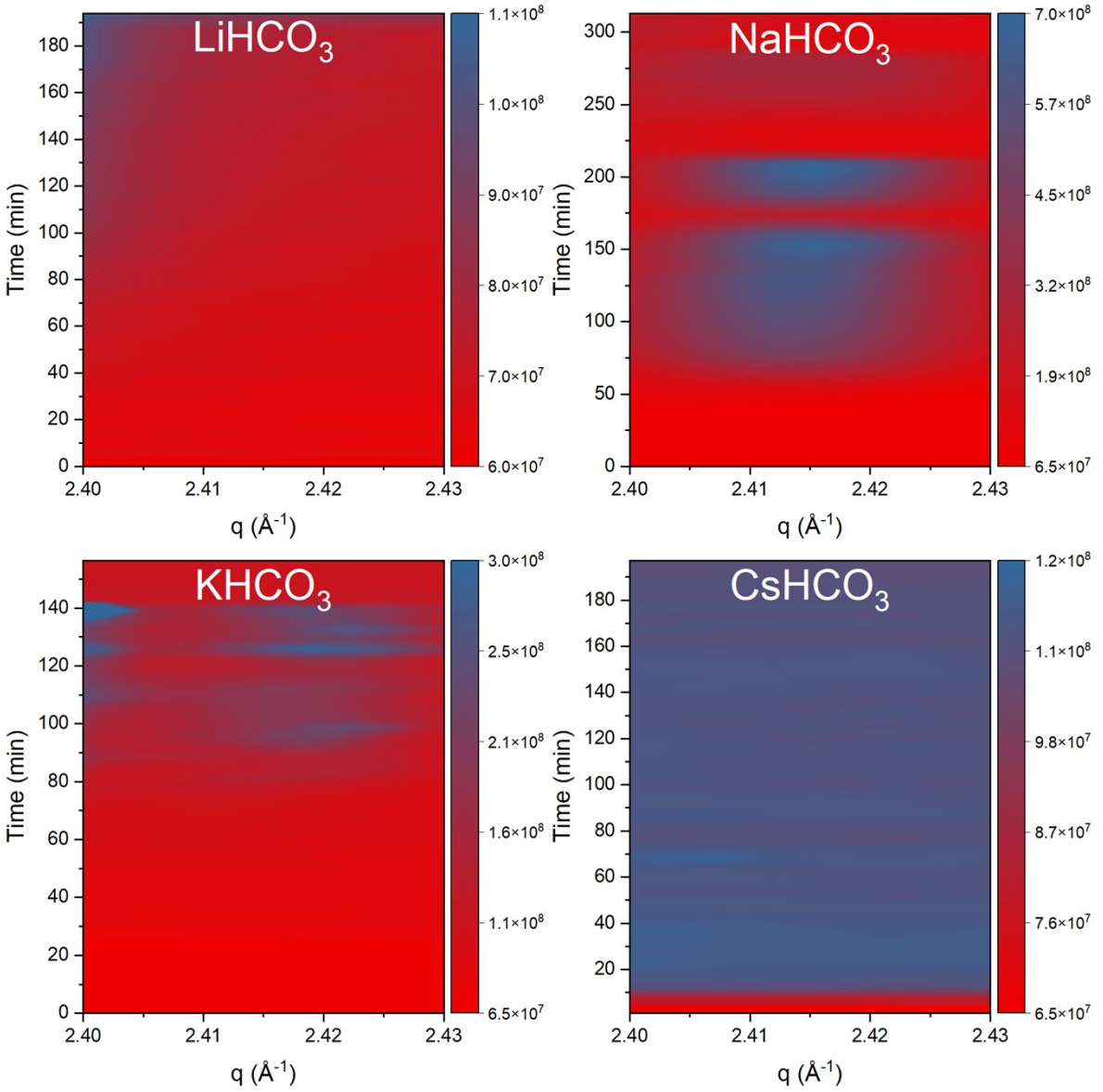

Figure S12. Analysis of the change in background signal (meaning a change in the electrolyte intensity) over electrolysis time right at the top of the catalyst layer in different alkali cations. All experiments were performed at 200 mA·cm^{-2}.

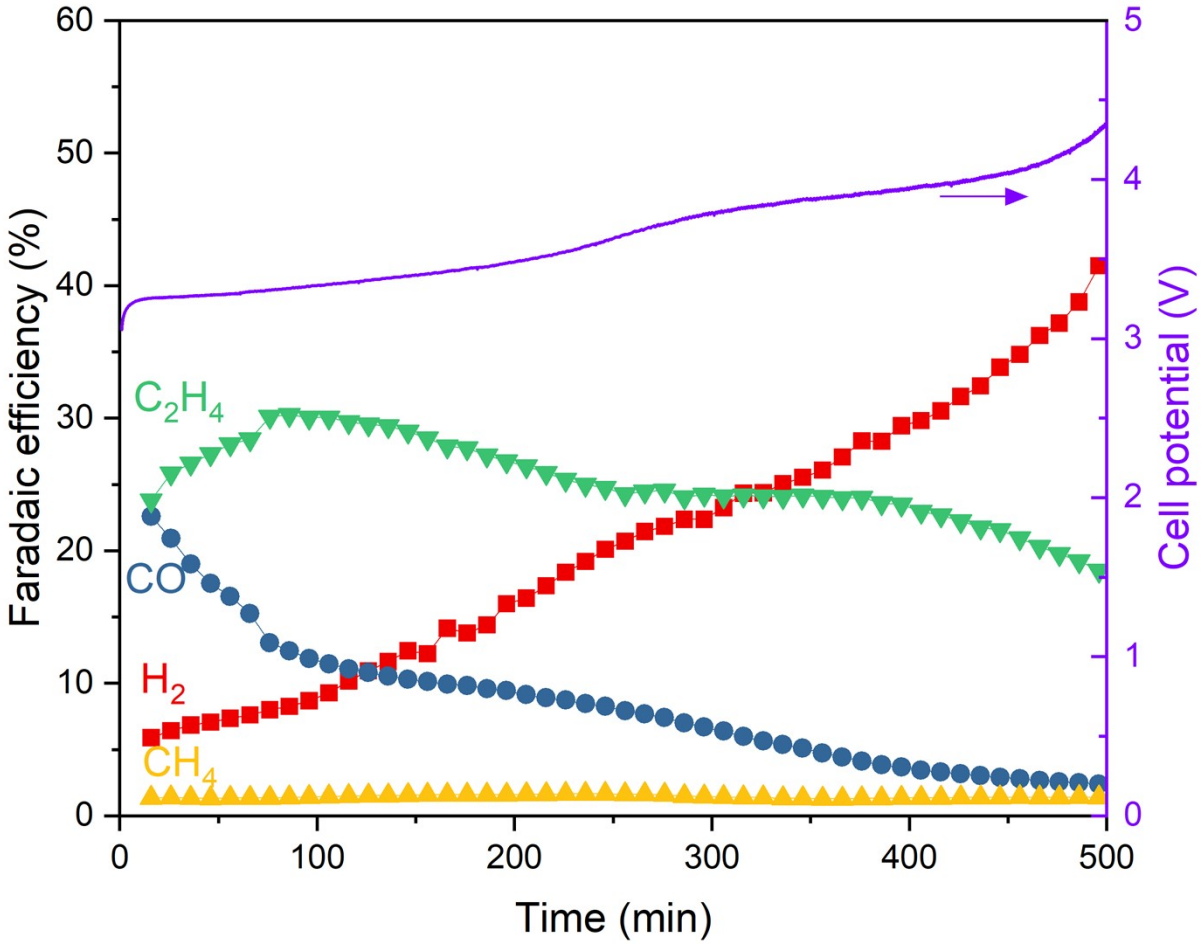

Figure S13. Changes in CO_2RR gaseous products and HER selectivity (left y-axis) and cell potential (right y-axis) over electrolysis time. The experiment was performed at 200 $mA \cdot cm^{-2}$ and in 0.1 M $CsHCO_3$ anolyte.

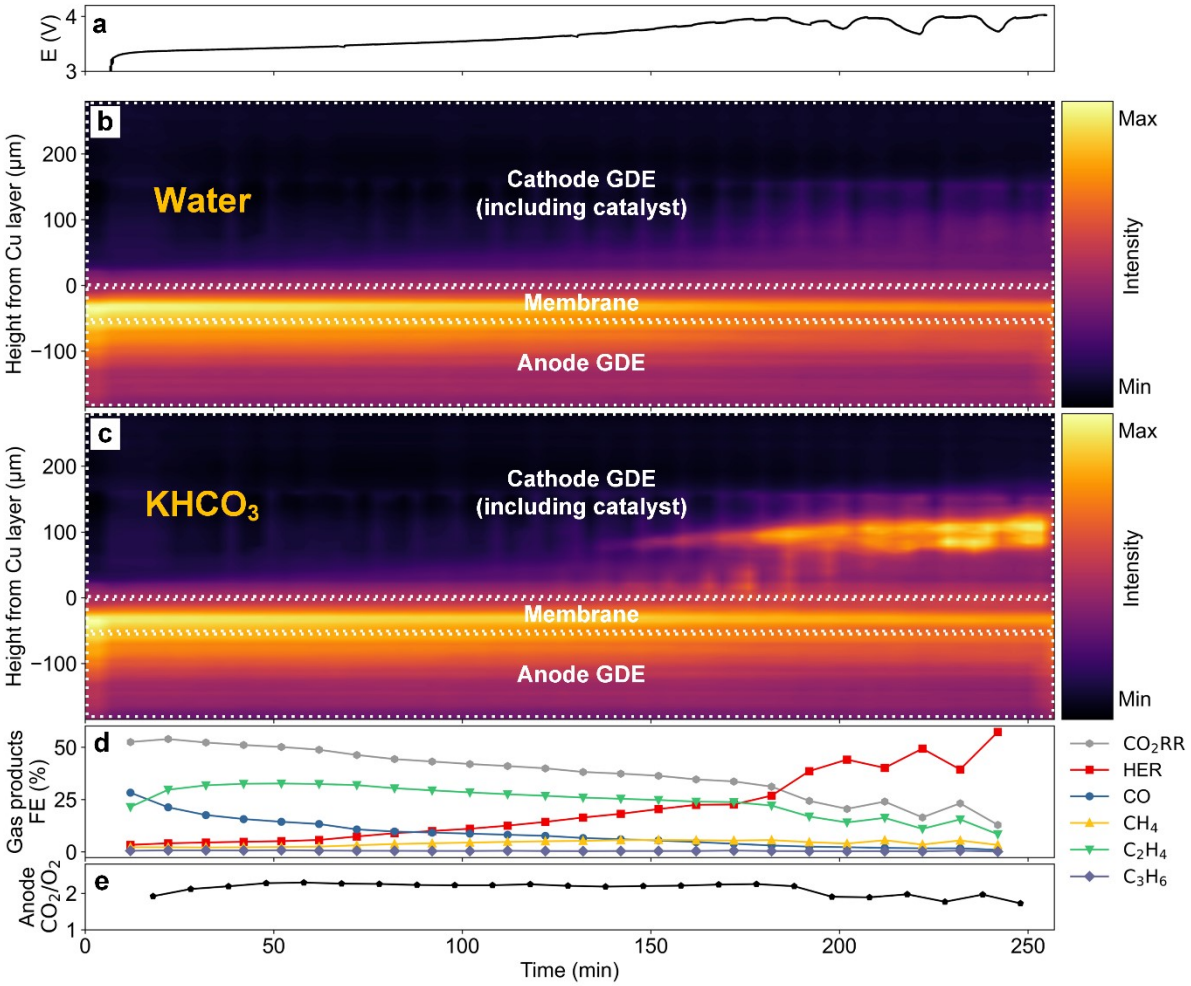

Figure S14. Changes in (a) cell potential, (b) electrolyte/water evolution, (c) salt precipitation, (d) gaseous CO_2RR/HER selectivity, and (e) CO_2/O_2 ratio at the anode in the MEA over electrolysis time. The experiment was performed at 200 mA·cm^{-2} and in 0.1 M $KHCO_3$ anolyte. The color intensities shown in (b) and (c) are not comparable with each other and should be treated separately. Detailed CO_2RR liquid product data is presented in Table S5.

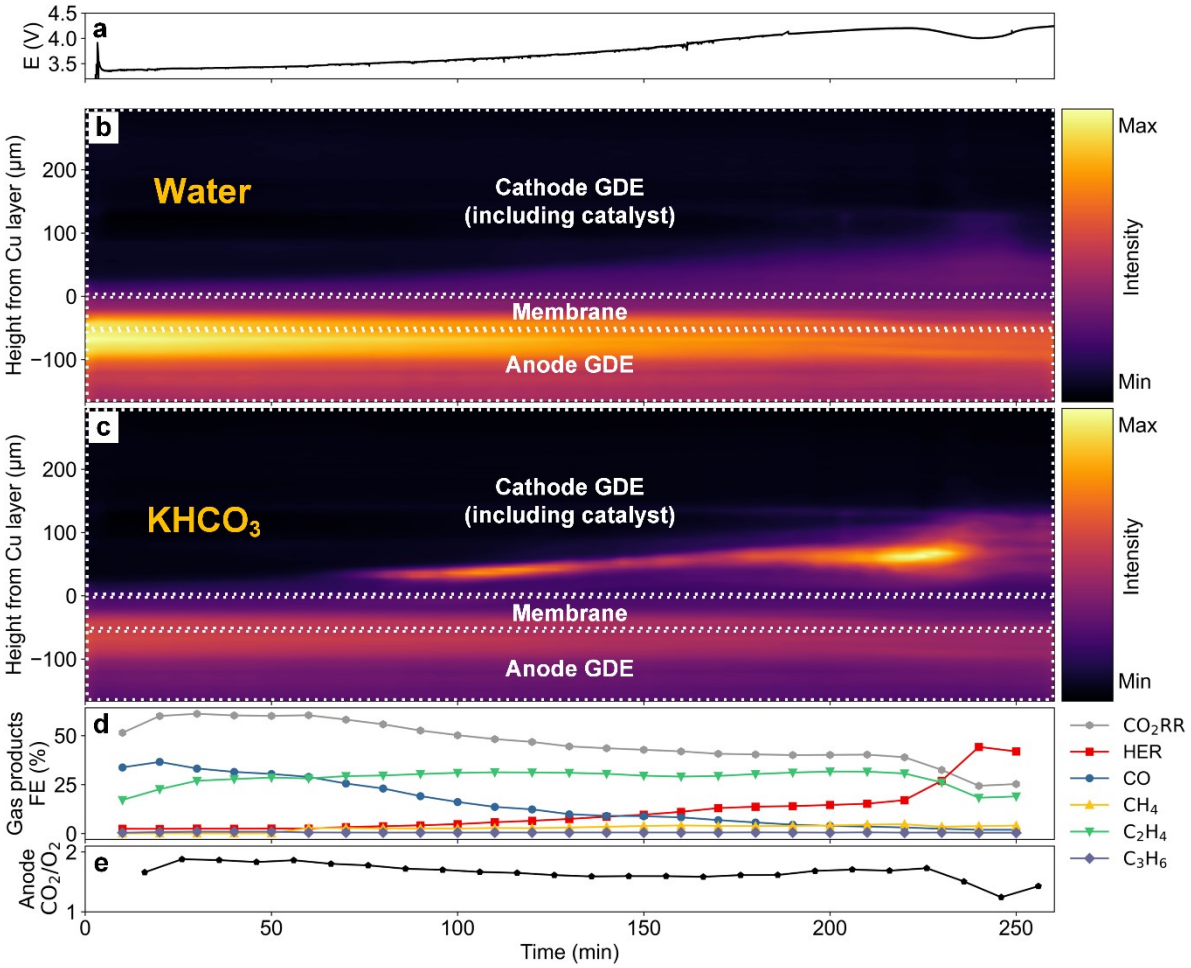

Figure S15. Changes in cell potential (top plot), electrolyte content and salt precipitation in the cathode GDE (middle heatmap plots), gaseous CO_2RR/HER selectivity (bottom plot) over electrolysis time. The experiment was performed at 200 mA·cm^{-2} and in 0.001 M $KHCO_3$ anolyte. Detailed CO_2RR liquid product data is presented in Table S6.

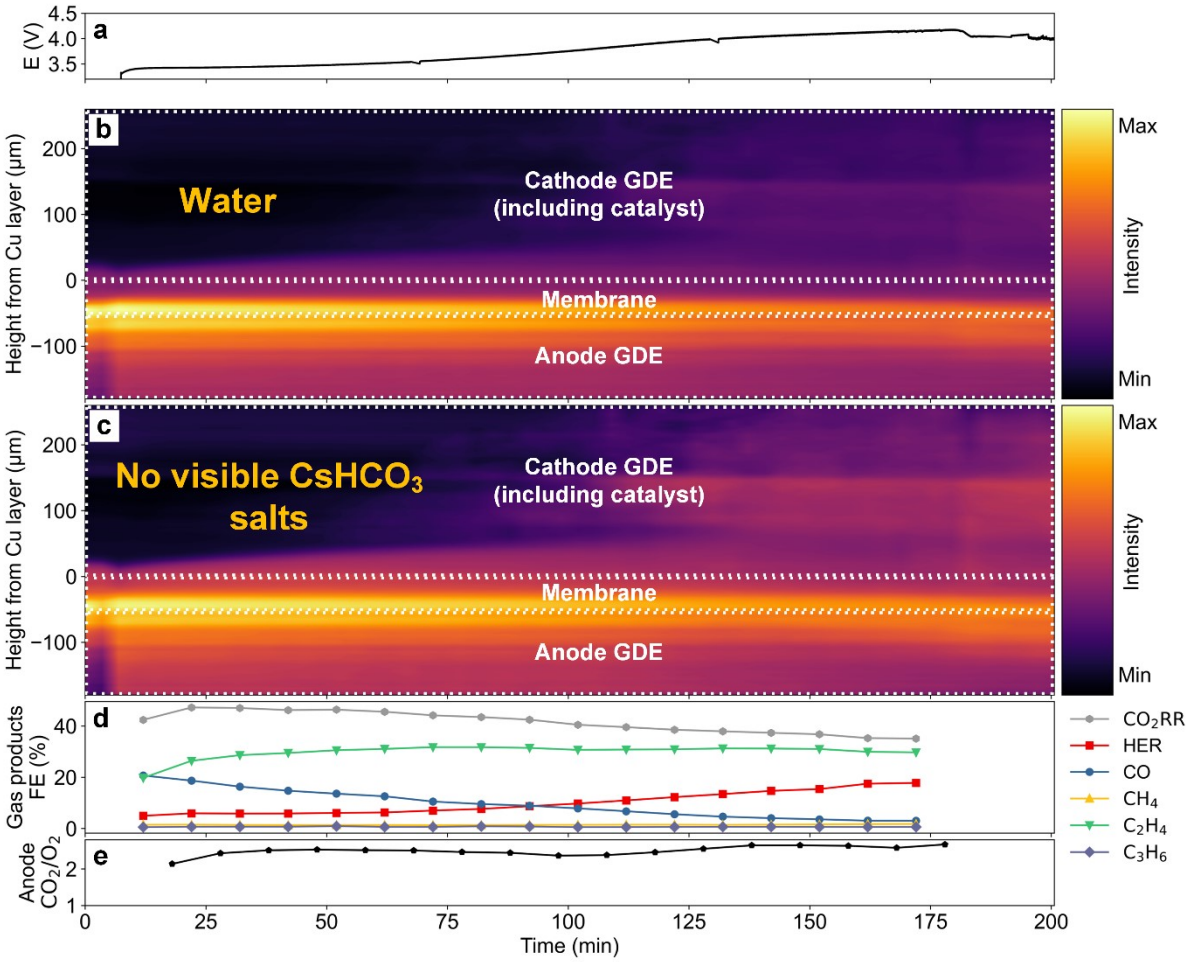

Figure S16. Changes in cell potential (top plot), electrolyte content and salt precipitation in the cathode GDE (middle heatmap plots), gaseous CO_2RR/HER selectivity (bottom plot) over electrolysis time. The experiment was performed at 200 mA·cm^{-2} and in 0.01 M $CsHCO_3$ anolyte. Detailed CO_2RR liquid product data is presented in Table S7.

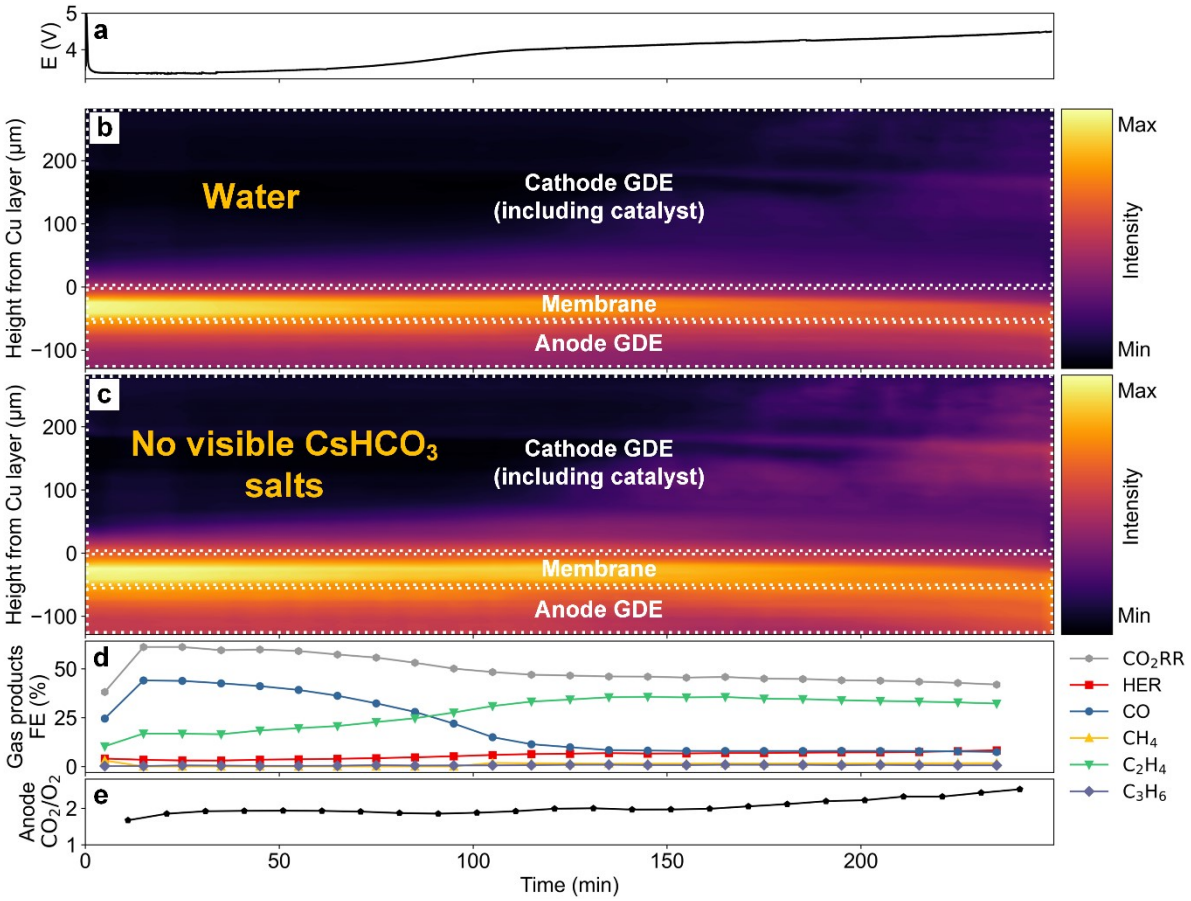

Figure S17. Changes in cell potential (top plot), electrolyte content and salt precipitation in the cathode GDE (middle heatmap plots), gaseous CO_2RR/HER selectivity (bottom plot) over electrolysis time. The experiment was performed at 200 $mA \cdot cm^{-2}$ and in 0.001 M $CsHCO_3$ anolyte. Detailed CO_2RR liquid product data is presented in Table S8.

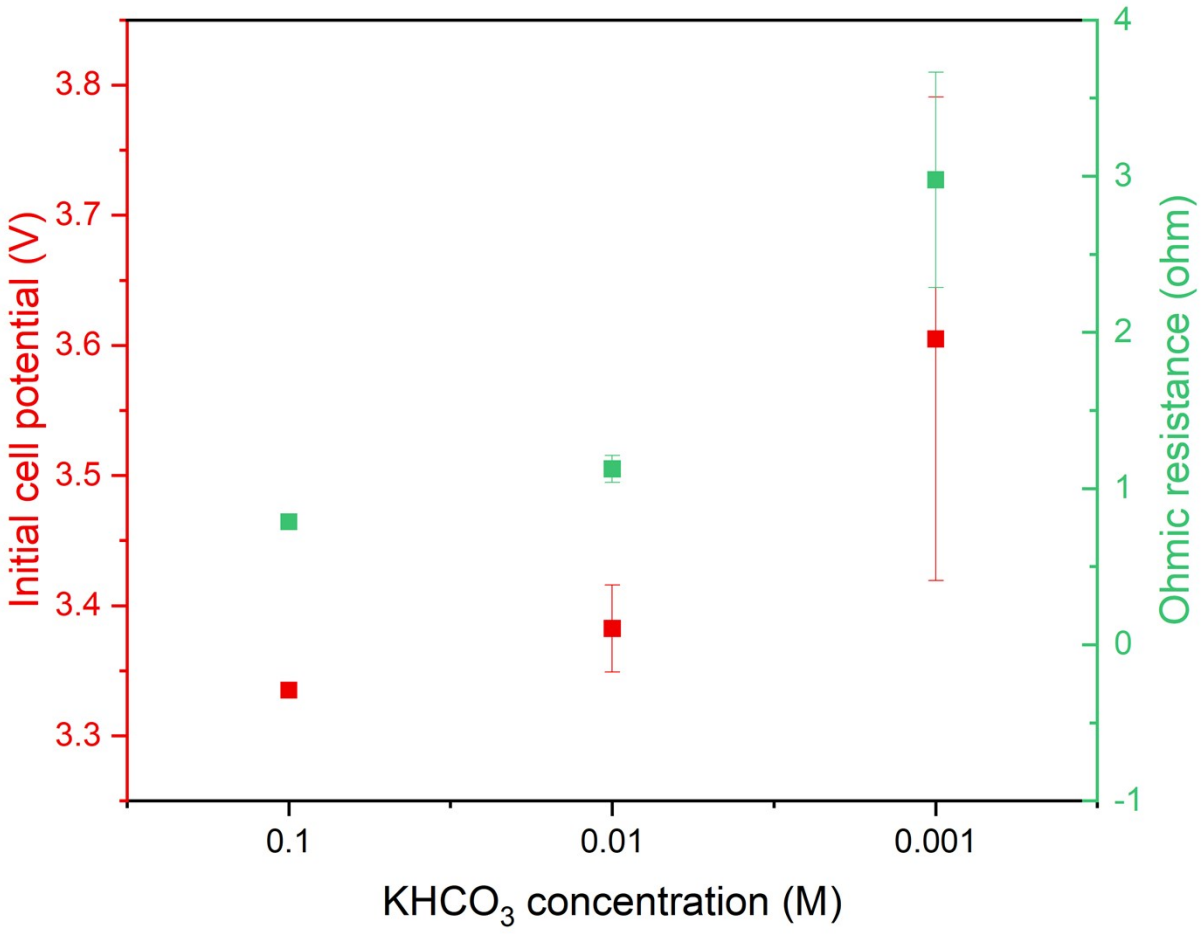

Figure S18. Changes in initial cell potential relate to changes in ohmic resistance (calculated via the current interrupt technique across the whole cell) at different $KHCO_3$ anolyte concentrations. All experiments were conducted at 200 $mA \cdot cm^{-2}$. The error bar shows the standard deviation from three separate measurements.

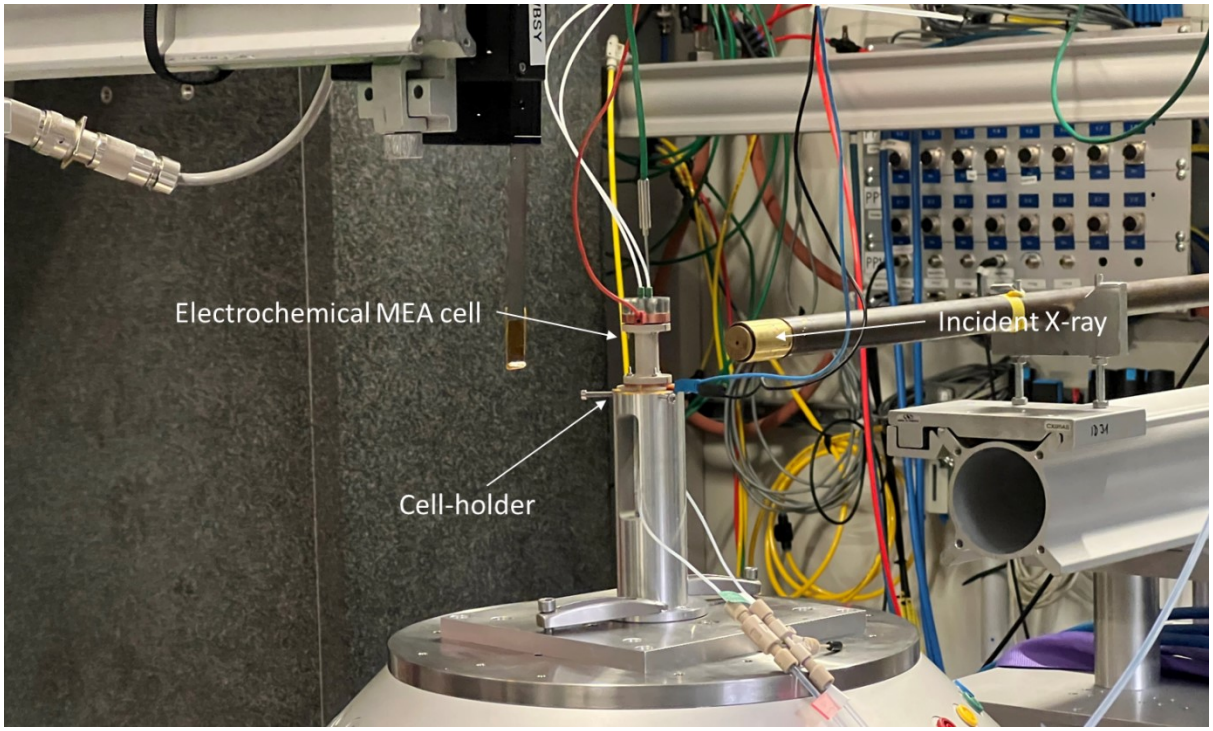

Figure S19. Digital photo of how the electrochemical cell was placed during X-ray measurement in front of the incident X-ray beam at ID 31, ESRF, France.

Tables

Table S1. Faradaic efficiency of liquid CO_2RR products (including both anode and cathode) in 0.1 M $LiHCO_3$ anolyte. The experiment was performed at 200 $mA \cdot cm^{-2}$ (for the experiment presented in Figure 3 of the main manuscript).

Liquid products	**Faradaic efficiency (%)**
Glycoaldehyde	0.03
Formate	0.08
Acetate	0
Ethylene Glycol	0.13
Hydroxyacetone	0
Acetaldehyde	0
Ethanol	0.04
Propanol	0
Sum	**0.27**

Table S2. Faradaic efficiency of liquid CO_2RR products (including both anode and cathode) in 0.1 M $NaHCO_3$ anolyte. The experiment was performed at 200 $mA \cdot cm^{-2}$ (for the experiment presented in Figure 4 of the main manuscript).

Liquid products	**Faradaic efficiency (%)**
Glycoaldehyde	0.02
Formate	1.14
Acetate	3.11
Ethylene Glycol	0
Hydroxyacetone	0.06
Acetaldehyde	0.12
Ethanol	3.15
Propanol	0.05
Sum	**7.65**

Table S3. Faradaic efficiency of liquid CO_2RR products (including both anode and cathode) in 0.1 M $KHCO_3$ anolyte. The experiment was performed at 200 $mA \cdot cm^{-2}$ (for the experiment presented in Figure S6 above).

Liquid products	**Faradaic efficiency (%)**
Glycoaldehyde	0.27
Formate	4.30
Acetate	13.29
Ethylene Glycol	0.18
Hydroxyacetone	0.12
Acetaldehyde	2.14
Ethanol	13.80
Propanol	1.72
Sum	**35.82**

Table S4. Faradaic efficiency of liquid CO_2RR products (including both anode and cathode) in 0.1 M $CsHCO_3$ anolyte. The experiment was performed at 200 $mA \cdot cm^{-2}$ (for the experiment presented in Figure 5 of the main manuscript and Figure S7 above).

Liquid products	**Faradaic efficiency (%)**
Glycoaldehyde	0.38
Formate	4.12
Acetate	12.53
Ethylene Glycol	0.32
Hydroxyacetone	0.09
Acetaldehyde	4.25
Ethanol	24.03
Propanol	4.75
Sum	**50.47**

Table S5. Faradaic efficiency of liquid CO_2RR products (including both anode and cathode) in 0.01 M $KHCO_3$ anolyte. The experiment was performed at 200 $mA \cdot cm^{-2}$ (for the experiment presented in Figure S9 above).

Liquid products	**Faradaic efficiency (%)**
Glycoaldehyde	0.25
Formate	3.44
Acetate	11.57
Ethylene Glycol	0.07
Hydroxyacetone	0.02
Acetaldehyde	2.15
Ethanol	14.78
Propanol	1.81
Sum	**34.09**

Table S6. Faradaic efficiency of liquid CO_2RR products (including both anode and cathode) in 0.001 M $KHCO_3$ anolyte. The experiment was performed at 200 $mA \cdot cm^{-2}$ (for the experiment presented in Figure S10 above).

Liquid products	**Faradaic efficiency (%)**
Glycoaldehyde	0.40
Formate	2.57
Acetate	10.95
Ethylene Glycol	0.04
Hydroxyacetone	0
Acetaldehyde	2.55
Ethanol	17.61
Propanol	1.15
Sum	**35.28**

Table S7. Faradaic efficiency of liquid CO_2RR products (including both anode and cathode) in 0.01 M $CsHCO_3$ anolyte. The experiment was performed at 200 $mA \cdot cm^{-2}$ (for the experiment presented in Figure S11 above).

Liquid products	**Faradaic efficiency (%)**
Glycoaldehyde	0.43
Formate	5.01
Acetate	11.69
Ethylene Glycol	0.35
Hydroxyacetone	0.11
Acetaldehyde	3.03
Ethanol	15.99
Propanol	3.47
Sum	**40.08**

Table S8. Faradaic efficiency of liquid CO_2RR products (including both anode and cathode) in 0.001 M $CsHCO_3$ anolyte. The experiment was performed at 200 $mA \cdot cm^{-2}$ (for the experiment presented in Figure S12 above).

Liquid products	**Faradaic efficiency (%)**
Glycoaldehyde	0.54
Formate	3.39
Acetate	6.21
Ethylene Glycol	0.16
Hydroxyacetone	0.04
Acetaldehyde	2.53
Ethanol	17.32
Propanol	3.89
Sum	**34.09**

References:

1. A. Xu, N. Govindarajan, G. Kastlunger, S. Vijay and K. Chan, *Accounts of Chemical Research*, 2022, **55**, 495-503.
2. S. Ringe, E. L. Clark, J. Resasco, A. Walton, B. Seger, A. T. Bell and K. Chan, *Energy & Environmental Science*, 2020, **13**, 646-647.
3. S. Nitopi, E. Bertheussen, S. B. Scott, X. Liu, A. K. Engstfeld, S. Horch, B. Seger, I. E. L. Stephens, K. Chan, C. Hahn, J. K. Nørskov, T. F. Jaramillo and I. Chorkendorff, *Chemical Reviews*, 2019, **119**, 7610-7672.
4. B. Endrődi, A. Samu, E. Kecsenovity, T. Halmágyi, D. Sebők and C. Janáky, *Nature Energy*, 2021, **6**, 439-448.
5. M. R. Singh, Y. Kwon, Y. Lum, J. W. Ager and A. T. Bell, *Journal of the American Chemical Society*, 2016, **138**, 13006-13012.
6. J. Resasco, L. D. Chen, E. Clark, C. Tsai, C. Hahn, T. F. Jaramillo, K. Chan and A. T. Bell, *Journal of the American Chemical Society*, 2017, **139**, 11277-11287.
7. S. Verma, X. Lu, S. Ma, R. I. Masel and P. J. A. Kenis, *Physical Chemistry Chemical Physics*, 2016, **18**, 7075-7084.
8. S. S. Bhargava, F. Proietto, D. Azmoodeh, E. R. Cofell, D. A. Henckel, S. Verma, C. J. Brooks, A. A. Gewirth and P. J. A. Kenis, *ChemElectroChem*, 2020, **7**, 2001-2011.
9. N. Gupta, M. Gattrell and B. MacDougall, *Journal of Applied Electrochemistry*, 2006, **36**, 161-172.
10. E. L. Clark and A. T. Bell, *Journal of the American Chemical Society*, 2018, **140**, 7012-7020.
11. T. Burdyny and W. A. Smith, *Energy & Environmental Science*, 2019, **12**, 1442-1453.
12. L.-C. Weng, A. T. Bell and A. Z. Weber, *Energy & Environmental Science*, 2019, **12**, 1950-1968.
13. K. P. Kuhl, E. R. Cave, D. N. Abram and T. F. Jaramillo, *Energy & Environmental Science*, 2012, **5**, 7050-7059.